

Charge-Transfer-Induced Lattice Collapse in Ni-Rich NCM Cathode Materials during Delithiation

Aleksandr O. Kondrakov,^{*,†,||} Holger Geßwein,^{§,#} Kristina Galdina,[⊥] Lea de Biasi,[†] Velimir Meded,[‡] Elena O. Filatova,[⊥] Gerhard Schumacher,[∇] Wolfgang Wenzel,[‡] Pascal Hartmann,^{†,||} Torsten Brezesinski,^{*,†,||} and Jürgen Janek^{†,○}

[†]Battery and Electrochemistry Laboratory, [‡]Institute of Nanotechnology, and [§]Institute for Applied Materials, Karlsruhe Institute of Technology, Hermann von Helmholtz Platz 1, 76344 Eggenstein Leopoldshafen, Germany

^{||}BASF SE, 67056 Ludwigshafen, Germany

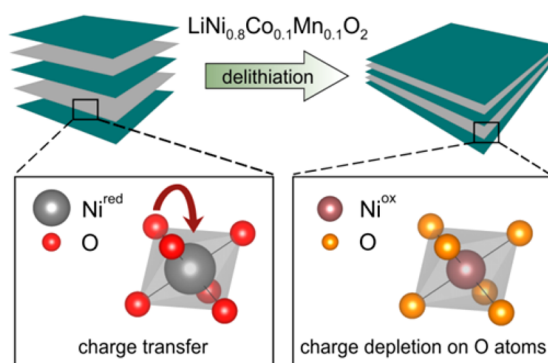
[#]Helmholtz Institute Ulm for Electrochemical Energy Storage, Helmholtzstr. 11, 89081 Ulm, Germany

[⊥]St. Petersburg State University, Ulyanovskaya Str. 1, 198504 St. Petersburg, Russia

[∇]Helmholtz Zentrum Berlin für Materialien und Energie, Hahn Meitner Platz 1, 14109 Berlin, Germany

[○]Institute of Physical Chemistry & Center for Materials Research, Justus Liebig University Giessen, Heinrich Buff Ring 17, 35392 Giessen, Germany

ABSTRACT: Ni rich $\text{LiNi}_x\text{Co}_y\text{Mn}_z\text{O}_2$ (NCM) cathode materials have great potential for application in next generation lithium ion batteries owing to their high specific capacity. However, they are subjected to severe structural changes upon (de)lithiation, which adversely affects the cycling stability. Herein, we investigate changes in crystal and electronic structure of NCM811 (80% Ni) at high states of charge by a combination of *operando* X ray diffraction (XRD), *operando* hard X ray absorption spectroscopy (hXAS), *ex situ* soft X ray absorption spectroscopy (sXAS), and density functional theory (DFT) calculations and correlate the results with data from galvanostatic cycling in coin cells. XRD reveals a large decrease in unit cell volume from 101.38(1) to 94.26(2) Å³ due to collapse of the interlayer spacing when $x(\text{Li}) < 0.5$ (decrease in c axis from 14.469(1) Å at $x(\text{Li}) = 0.6$ to 13.732(2) Å at $x(\text{Li}) = 0.25$). hXAS shows that the shrinkage of the transition metal–oxygen layer mainly originates from nickel oxidation. sXAS, together with DFT based Bader charge analysis, indicates that the shrinkage of the interlayer, which is occupied by lithium, is induced by charge transfer between O 2p and partially filled Ni e_g orbitals (resulting in decrease of oxygen–oxygen repulsion). Overall, the results demonstrate that high voltage operation of NCM811 cathodes is inevitably accompanied by charge transfer induced lattice collapse.



INTRODUCTION

$\text{LiNi}_{0.8}\text{Co}_{0.1}\text{Mn}_{0.1}\text{O}_2$ (NCM811) is one of the most promising cathode materials among the redox active layered lithium transition metal (TM) oxides owing to its high specific capacity (up to 200 mAh/g at 4.6 V vs Li^+/Li).¹ However, significant capacity fading and low structural stability at high voltages limit the stable operating range of NCM811 based cells in practical applications.^{2,3} Recent studies have demonstrated that the capacity fading is strongly related to the mechanical disintegration of secondary particles.^{4,5} The lattice changes of primary particles during (de)lithiation are anisotropic and cause mechanical strain at the grain boundaries resulting in material fracture. Particularly, the interlayer spacing, i.e., the distance between the basal and upper oxygen planes of adjacent transition metal–oxygen (TM O) layers, where the Li ions are accommodated, is subjected to severe nonmonotonic changes

at voltages above 4.0 V vs Li^+/Li .^{5–8} These variations are determined by changes occurring in the TM O and lithium–oxygen (Li O) slabs (they alternate across the z direction of the layered NCM lattice).⁹ However, the low X ray scattering factor of oxygen makes determination of its unit cell position (z coordinate) challenging, and in the literature, there is limited information on the crystallographic changes in these layers.^{5,10} Hard X ray absorption spectroscopy (hXAS) performed on isostructural compounds shows that the TM O layers shrink monotonically due to continuous TM oxidation.^{11–14} The behavior of the interlayer (Li O slabs) is less understood and is treated only in few theoretical and experimental studies.^{5,9,15} It

is believed that lithium screens the repulsion between the oxygen planes, which should result in linear expansion of the Li O slabs during delithiation.⁹ However, reports on mixing (overlap) between TM and oxygen bands in Ni rich lithium transition metal oxides suggest a high degree of covalency of the TM O bond.^{16,17} These findings, together with soft X ray absorption spectroscopy (sXAS) data on the O K edge for various isostructural materials, e.g., LiCoO₂,^{18,19} LiNi_{0.65}Co_{0.25}Mn_{0.1}O₂,²⁰ Li_{1-x}Ni_{0.33}Co_{0.33}Mn_{0.33}O₂,²¹ Li_{1.2}Ni_{0.2}Mn_{0.6}O₂,²² and Li_{1.16}Ni_{0.15}Co_{0.19}Mn_{0.50}O₂,²³ indicate that the effective charge on the O atoms may vary with the TM redox state. Such charge variations will inevitably affect the oxygen–oxygen repulsion, which is essential for maintaining the layered crystalline structure. Given the apparent high degree of TM O band mixing expected for NCM811 and the lack of experimental data, a thorough investigation of changes in electronic structure of both the TMs and oxygen during cycling and their effect on the lattice is an important issue.

In the present work, we study changes in crystal and electronic structure of NCM811 during delithiation via *operando* X ray diffraction (XRD) and hXAS as well as *ex situ* sXAS and density functional theory (DFT) with Bader charge analysis. We examine crystallographic changes, particularly in the TM O and Li O slabs, and correlate the data with the redox state of TMs from hXAS. Furthermore, we complement the results by sXAS data obtained at different states of charge and supporting DFT results for charge analysis. The high selectivity of a dipole allowed 1s–2p transition in the O K edge allows for direct probing of the unoccupied 2p states and provides information on the effective charge of the oxygen atoms.²⁴

■ EXPERIMENTAL SECTION

Electrochemical Testing. Both the electrolyte (1 M LiPF₆ in ethylene carbonate and dimethyl carbonate, 3:7 by weight) and the NCM811 based electrodes, with 94 wt % active material, were obtained from BASF SE. Galvanostatic cycling tests were performed at 25 °C on coin cells containing NCM811 cathode, glass microfiber film separator (Whatman GF/D, GE Healthcare Life Sciences), Li metal anode (Rockwood Lithium Inc.), and 250 μL of electrolyte by use of a MACCOR Series 4000 cyler (Tulsa).

X-ray Diffraction and X-ray Absorption Spectroscopy. *Operando* XRD measurements were performed at 25 °C on NCM811/Li pouch cells using a high intensity laboratory Mo Kα_{1,2} diffractometer.²⁵ Details on the setup as well as the description of calibration procedures can be found elsewhere.⁵ XRD patterns (2θ = 5–37°, Mo Kα_{1,2}) were collected every 150 s with cycling in the voltage range between 3.0 and 4.6 V at a rate of C/20. Structural refinement was done with TOPAS–Academic V5 software using the previously described procedure.⁵

Operando hXAS measurements of the TM K edges were performed on beamline P65 at HASYLAB at DESY. The cell, equipped with 2 mm polyimide windows, was measured in transmission mode under the same cycling conditions used for XRD. Powder reference samples (NiO, LiNiO₂, CoO, LiCoO₂, Mn₂O₃, and MnO₂) were ground, brushed onto polyimide tape, and sealed under argon atmosphere prior to measuring. Alignment, background subtraction, and data normalization were done using the Demeter software package.²⁶

Ex situ sXAS measurements were carried out in total electron yield (TEY) mode at the RGLB beamline (BESSY II) at Helmholtz Zentrum Berlin (HZB).²⁷ To this end, NCM811

cathodes were delithiated, then extracted from Li cells inside an argon filled glovebox, washed with dimethyl carbonate, dried, and finally manually polished to remove surface impurities. All samples were sealed, stored, and transported under an argon atmosphere. Spectral shifts caused by the monochromator or beam instabilities were corrected for by measuring photo emission spectra of Au foil prior to each sXAS run.

Density Functional Theory. Settings used for DFT calculations were largely default, including the PBE exchange correlation functional.²⁸ The convergence criterion was set to 10⁻⁵ eV. A 5 × 5 × 1 Monkhorst–Pack k points mesh was utilized together with Grimme correction, which was used to address any possible van der Waals interactions between the layers.^{29,30} The construction of the geometries is based on experimental XRD data. Because exact positions for the lithium vacancies at *x*(Li) < 1 are not known, the lithium atoms were removed in such a manner that the highest possible crystal symmetry was retained. Overall, this gave a unique solution for all structures. The geometries are provided in plain text format (VASP input data) in the [Supporting Information](#).

■ RESULTS AND DISCUSSION

Cycling Performance. Figure 1a depicts the capacity retention over 50 cycles of NCM811/Li cells charged to

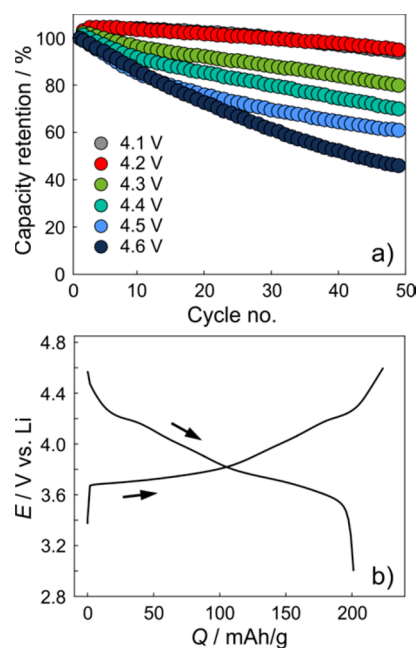


Figure 1. (a) Capacity retention at C/2 for NCM811/Li cells charged to different cutoff voltages and (b) representative charge/discharge curves at C/10.

different cutoff voltages. The cells underwent a formation cycle at 25 °C and C/10 between 3.0 V (note that the voltage is given with respect to Li⁺/Li in the following) and either 4.1, 4.2, 4.3, 4.4, 4.5, or 4.6 V, and they were then cycled at C/2 in the chosen voltage range for the subsequent cycles. We note that electrolyte decomposition, particularly at high voltages, adversely affects the cell performance, among others, by consumption of active lithium and formation of a cathode solid electrolyte interface (SEI) layer.^{31,32} To minimize these effects, the NCM811 cathodes were cycled in half cells without potentiostatic steps at the cutoff voltages. Nevertheless, the

capacity fading is virtually enhanced at such conditions because overpotentials arising during cycling, e.g., due to material fracture, lower the actual cell voltage. Thus, the data shown in Figure 1a reflect the “worst case performance” when compared with the typical cyclability of NCM811/graphite cells (Figure S1), yet the Coulombic efficiency stabilized above 98% after the formation cycle, thus indicating rather stable electrolyte behavior. As can be seen, increasing the cutoff voltage from 4.1 to 4.2 V barely affects the capacity retention, but leads to an increase in specific discharge capacity from 148 to 167 mAh/g (see also Table 1). Further increasing the cutoff voltage

Table 1. First Cycle Discharge Capacity at C/10 and Specific Capacity Loss Per Cycle at C/2 for NCM811/Li Cells Charged to Different Cutoff Voltages

E_{cutoff} (V)	discharge capacity (mAh/g)	capacity loss (mAh/g)
4.1	148	0.4
4.2	167	0.4
4.3	188	0.7
4.4	197	0.8
4.5	200	0.9
4.6	201	1.2

improves the initial discharge capacity, but dramatically impairs the cycling stability. The specific capacity loss per cycle is found to be 1.75, 2, 2.25, and 3 times higher for cells charged to 4.3, 4.4, 4.5, and 4.6 V, respectively, than those cycled between 3.0 V and 4.1 or 4.2 V. The voltage profile shown in Figure 1b reveals a significant change in slope over these voltages, eventually evolving to a subtle plateau. This plateau spreads up to 4.27 V and is characteristic of lithium transition metal oxides with a high Ni content such as LiNiO_2 , which exhibits a series of phase transitions in this voltage range.^{33,34} Overall, both this resemblance and the data in Figure 1 and Table 1 suggest that

increasing the cutoff voltage on charge above 4.2 V results in large structural changes, which (besides the above mentioned enhanced electrolyte degradation) dramatically lower the stability of the NCM811 cathode material.

Lattice Changes. In our previous work, we found that high Ni NCMs suffer from significant first cycle irreversibilities (up to 14%), resulting in partial active lithium loss and delayed change in lattice parameters in the initial charge cycle.⁵ Thus, for better correlation of the lattice parameter changes with lithium content, precycled cells (at 25 °C and C/10 between 3.0 and 4.3 V) were used here for XRD. Figure 2a depicts a contour plot of *operando* XRD patterns obtained on a NCM811/Li cell cycled at C/20 between 3.0 and 4.6 V, with a constant voltage step for 1 h at the end of charge (see also Figure S2 for contour plot of peak intensities and representative XRD patterns). In agreement with literature reports, the crystal structure can be described by the space group $R\bar{3}m$.^{6,8} Because the lattice changes upon charge and discharge are reversible, in the following, we only focus on those occurring in the charge cycle and discuss them with respect to lithium content (estimated from current and charging time).

Figure 2b shows the decrease in unit cell volume from 101.38(1) to 94.26(2) Å³ (at $x(\text{Li}) = 0.25$) with delithiation. This contraction occurs in a nonlinear manner. At the beginning of the charge cycle, the unit cell volume decreases slowly until a lithium content of $x(\text{Li}) \approx 0.5$ is reached. Then, the volume decreases much faster, and for $x(\text{Li}) < 0.4$, it decreases virtually linearly and steeply with lithium content until the end of charge. The unit cell volume is determined by the lattice parameters a and c , which are affected by the intralayer spacing and slab heights, respectively. As can be seen from Figure 2c, the a lattice parameter exhibits an almost linear drop from 2.8661(1) to 2.8211(1) Å (at $x(\text{Li}) = 0.5$) and then levels off at 2.8153(1) Å (at $x(\text{Li}) = 0.25$). Interestingly, the initial decrease in unit cell volume bears some resemblance to

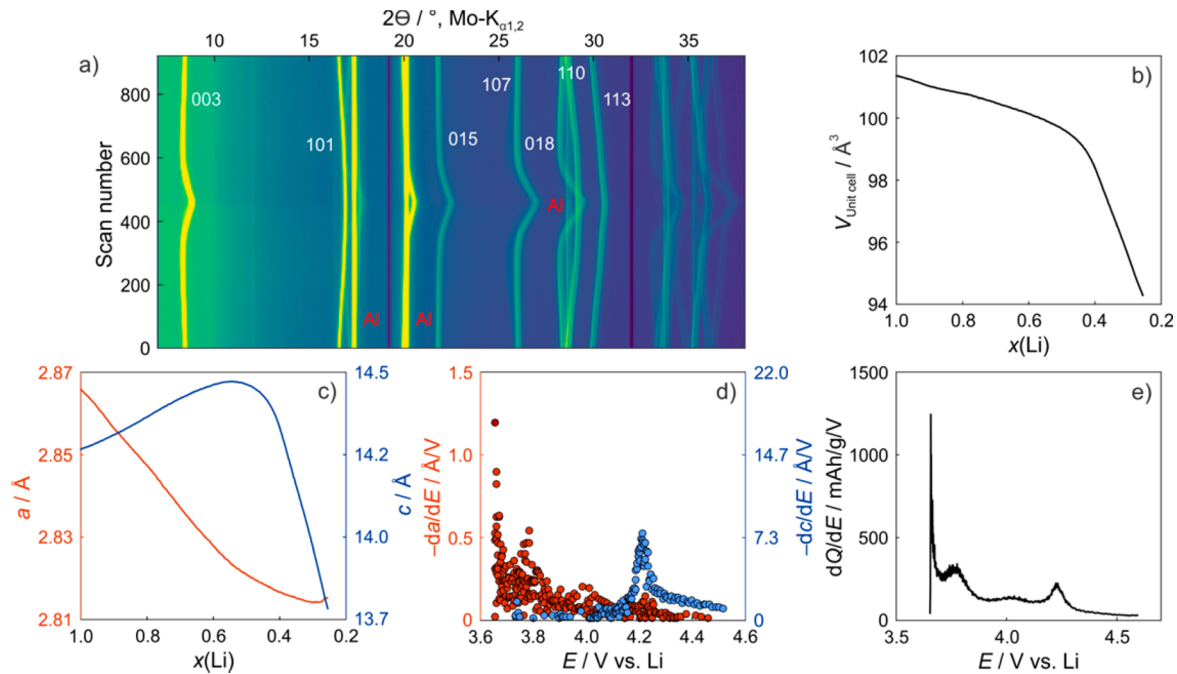


Figure 2. (a) Contour plot of *operando* XRD patterns obtained on a NCM811/Li cell, together with structural refinement results (b, c) as well as differential lattice parameter (d) and capacity curves (e). The changes in unit cell volume and lattice parameters a and c versus the lithium content are shown in (b) and (c), respectively.

the initial decrease in a . Although the absolute changes are significantly smaller than those observed for c , the a lattice parameter contributes to the cell volume by the second power ($V = a^2c \sin \pi/3$), and therefore determines the magnitude of the changes in this region (at high lithium content). The c lattice parameter exhibits much more complex behavior, showing an initial increase from 14.249(1) to 14.469(1) Å (at $x(\text{Li}) = 0.6$), followed by a broad maximum and finally a steep decrease to 13.732(2) Å (at $x(\text{Li}) = 0.25$). The latter drop is strongly reminiscent of that observed for the unit cell volume at $x(\text{Li}) \leq 0.5$. This feature, together with the fact that the lattice parameter a barely changes in this region, establishes that the unit cell volume is mainly controlled by the c lattice parameter when $x(\text{Li}) \leq 0.5$.

To correlate the observed structural behavior with the capacity retention data in Figure 1a, we analyzed the rates of the lattice parameter changes (variations in slope) as a function of cell voltage (E). This means we took derivatives of the lattice parameters a and c with respect to E to obtain da/dE and dc/dE curves (Figure 2d). These were then used to determine those voltage regions, where the changes in lattice parameters are most pronounced. Examination of the da/dE profile revealed an extremum centered at 3.75 V. Interestingly, both its shape and position correlate well with the main maximum seen in the differential capacity curve (dQ/dE) in Figure 2e. The dc/dE profile shows an extremum at 4.2 V, which strongly resembles the second largest maximum in the differential capacity curve at the same voltage. These correlations indicate that the structural changes are connected to redox processes, and we will discuss them in the following sections. However, we like to recall the capacity retention data and note that the largest changes in lattice parameter c occur at the voltage corresponding to the accelerated capacity fading. As mentioned above, the large decrease in c causes the significant contraction of unit cell volume (making >70% of the total change); therefore, we first discuss the nature of these lattice variations in more detail.

The c lattice parameter consists of the heights of the Li O ($h_{\text{Li-O}}$) and TM O slabs ($h_{\text{TM-O}}$), which alternate along the z direction (Figure 3a). Calculating $h_{\text{TM-O}}$ and $h_{\text{Li-O}}$ requires

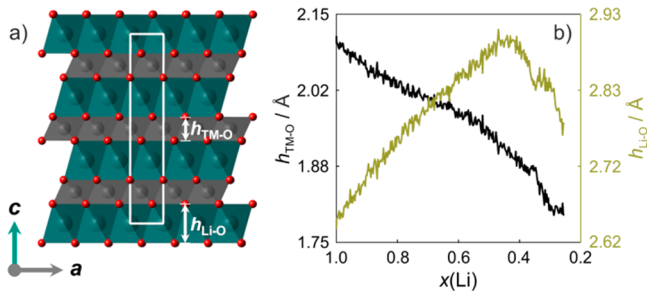


Figure 3. (a) Crystal structure of NCM811 with highlighted transition metal–oxygen layers (gray) and lithium interlayers (green) as well as TM O ($h_{\text{TM-O}}$) and Li O slab heights ($h_{\text{Li-O}}$). The unit cell is indicated by a white rectangle. (b) $h_{\text{TM-O}}$ and $h_{\text{Li-O}}$ versus the lithium content.

precise determination of the oxygen z coordinate (z_{O}), which may be prone to refinement faults (especially for data collected in short time periods) because of the low X ray scattering factor of oxygen. To overcome this limitation, the initial z_{O} value (used for refinement of the *operando* XRD patterns) was determined by neutron diffraction on pristine NCM material, as described elsewhere.⁵ Figure 3b shows the changes in slab

heights as a function of lithium content. The $h_{\text{TM-O}}$ value decreases from 2.111(1) to 1.797(2) Å during the course of delithiation. In contrast, $h_{\text{Li-O}}$ increases from 2.639(1) to 2.889(2) Å (at $x(\text{Li}) = 0.5$) and then decreases to 2.767(1) Å (at $x(\text{Li}) = 0.25$). Thus, at the beginning of delithiation, $h_{\text{TM-O}}$ and $h_{\text{Li-O}}$ evolve in opposite directions, corresponding to simultaneous shrinkage and expansion of the TM O and Li O slabs, respectively. The net effect of these changes on the c value is still positive in this region due to the fact that the expansion of the Li O slabs is more pronounced (0.250(3) vs 0.181(3) Å). Accordingly, the significant drop in c lattice parameter and the resulting unit cell volume changes are caused by the simultaneous decrease in both slab heights at $x(\text{Li}) < 0.5$ (more rigorously at $x(\text{Li}) < 0.45$). These results clearly demonstrate a strong correlation between the material stability and the crystallographic changes along the c axis. In the following, we analyze the structural changes in the TM O and Li O slabs in terms of redox processes.

Transition Metal K-Edge Evolution. Figure 4 shows Ni, Co, and Mn K edge hXAS spectra obtained *in operando* on a NCM811/Li cell. The nickel spectrum exhibits a broad absorption maximum at 8352 eV and a subtle pre edge at 8330 eV, whose shapes do not show significant changes with delithiation. The edge corresponds to the dipole allowed $1s-4p$ transition, while the pre edge corresponds to a formally forbidden $1s-3d(-4p)$ transition, typically arising in distorted octahedral TM sites.¹⁵ The positions of both the edge and pre edge shift with decreasing $x(\text{Li})$ from 8341 to 8344 eV and from 8330 to 8332 eV, respectively. Overall, these shifts toward higher energy are indicative of nickel oxidation.^{13,14} The initial position is located between the nickel K edge in NiO and LiNiO_2 , thus suggesting a mixed Ni(II/III) oxidation state, which evolves to Ni(III/IV) during the charge cycle (Figure S3).

The cobalt spectrum reveals an absorption maximum at 7730 eV and a pre edge located at 7710 eV. The initial edge position is higher in energy than that of CoO and close to LiCoO_2 , thus suggesting the Co(III) oxidation state (Figure S3). The derivative absorbance curves in Figure 4 further indicate that delithiation leads to distinct changes in Co K edge shape. However, both the shape and position of the pre edge remain virtually unaffected.

The manganese spectrum exhibits an absorption maximum at 6559 eV and a pre edge around 6541 eV. However, differences among the sample and reference edge shapes do not allow unambiguous determination of the oxidation state but point at Mn(IV) (Figure S3). Similar to the cobalt data, the manganese spectra exhibit significant K edge shape variations and no notable shifts in pre edge features, thus indicating changes in local environment with decreasing $x(\text{Li})$.^{15,23} These findings are corroborated by the changes observed in the L edge spectra (see L_3 to L_2 peak ratio in Figure S4) and agree with previous studies on isostructural lithium transition metal oxides.^{18–23} However, we note that our data only demonstrate clear nickel redox activity. Redox activity of cobalt and manganese, previously reported for $\text{LiNi}_{0.33}\text{Co}_{0.33}\text{Mn}_{0.33}\text{O}_2$,^{35,36} $\text{LiNi}_{0.5}\text{Mn}_{0.5}\text{O}_2$,³⁷ $\text{LiNi}_{0.5}\text{Co}_{0.2}\text{Mn}_{0.3}\text{O}_2$,³⁸ $\text{LiNi}_{0.2}\text{Co}_{0.7}\text{Mn}_{0.1}\text{O}_2$,³⁹ and $\text{LiNi}_{0.45}\text{Co}_{0.45}\text{Mn}_{0.1}\text{O}_2$,⁴⁰ has not been observed.

Collectively, the hXAS results provide clear evidence of the contribution of nickel to the charge compensation during electrochemical cycling. Because the Ni content is high, we do not observe signs of exhaustion of nickel redox activity at high states of charge, as previously reported for Li

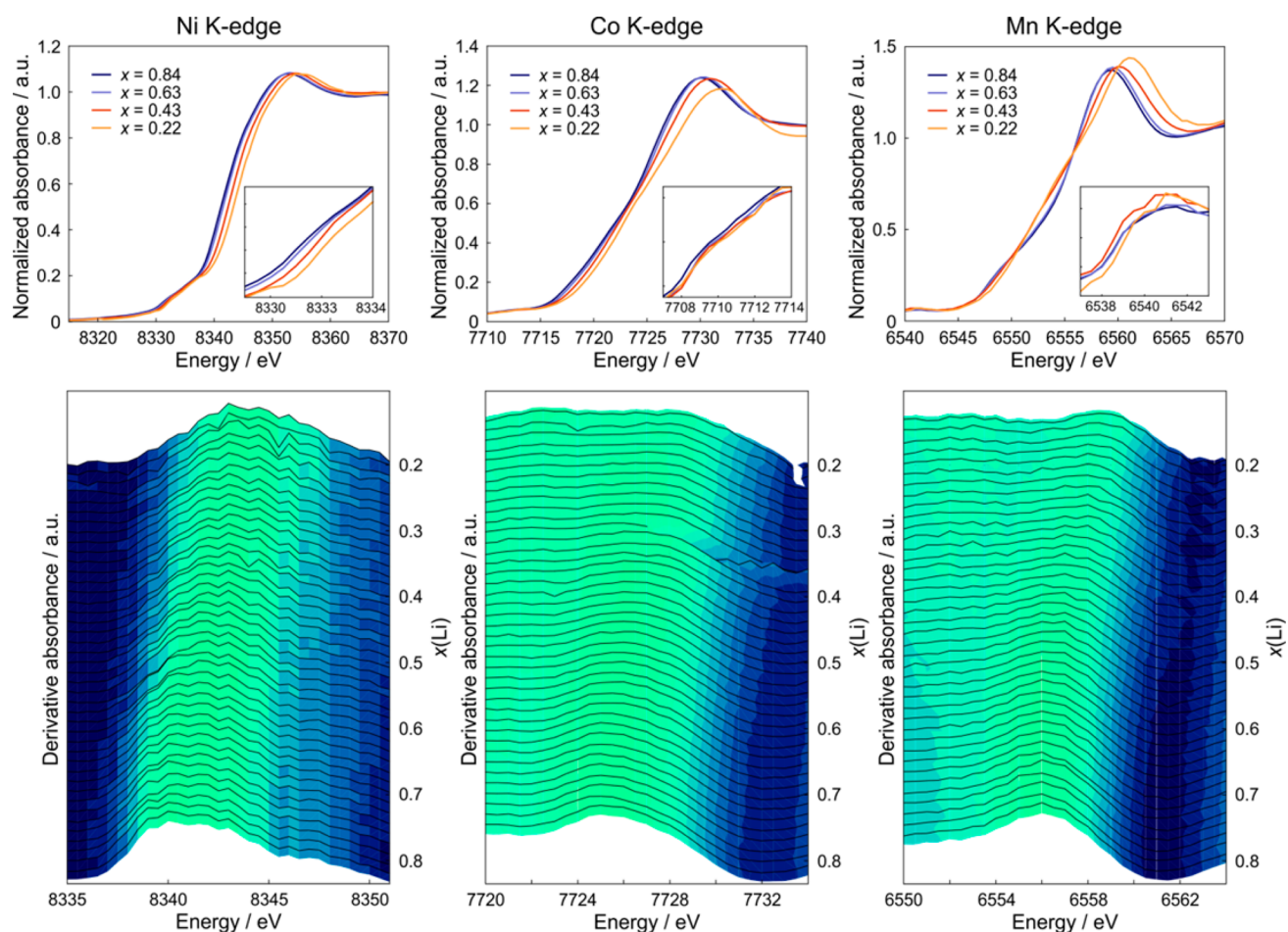


Figure 4. Operando Ni, Co, and Mn K edge hXAS spectra obtained on a NCM811/Li cell during the charge cycle (top) and first derivative absorbance curves (bottom).

$\text{Ni}_{0.33}\text{Co}_{0.33}\text{Mn}_{0.33}\text{O}_2$ (NCM111).¹⁴ Instead, nickel is continuously oxidized over the whole $x(\text{Li})$ range. Assuming that cobalt and manganese remain in their initial oxidation states and nickel changes by 0.8 charge units, we obtain 12% difference in nickel ionic radius, which qualitatively agrees with the 15% decrease in $h_{\text{TM-O}}$ from XRD. Such correlation suggests that the shrinkage of the TM O slabs occurs due to oxidation of nickel to higher states (for charge compensation reasons).

Oxygen K-Edge Evolution. To gain more insight into the mechanism that triggers the changes in the Li O slabs during delithiation, we analyzed the evolution of the O K edge using *ex situ* sXAS in TEY mode. It should be noted that the probing depth is limited to around 100 Å, and the results may be affected by byproducts formed in side reactions.⁴¹ Nevertheless, direct comparison with spectra of different reference materials indicates that the cathode surface in pristine and delithiated states is free of contaminants (besides the electrode additives, i.e., conductive carbon black and polyvinylidene fluoride binder) and in good agreement with the parent LiNiO_2 structure (Figure S5). In view of the reversibility of the observed spectral changes, we only discuss the charge cycle in the following (see Figure S6 for full charge/discharge cycle).

The O K edge spectra of the pristine and delithiated NCM811 cathode are shown in Figure 5. The relative intensities are normalized to the continuum jump at the photon energy of 576 eV after background subtraction (by extrapolation from the linear region below the onset of

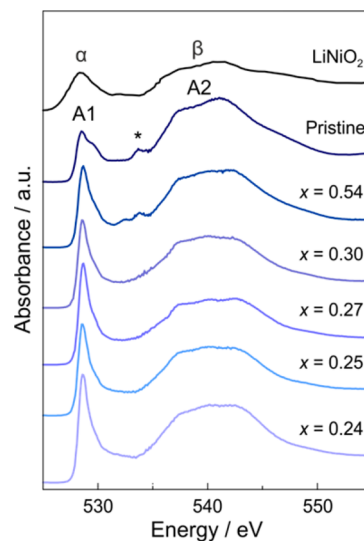


Figure 5. *Ex situ* O K edge sXAS spectra obtained on NCM811 in pristine and delithiated states.

absorption). This process normalizes the spectra to the same total oscillator strength, thus allowing direct comparison of spectral features among the data and, more importantly, quantitative analysis.⁴² The spectrum of pristine NCM811 well resembles that of the parent LiNiO_2 , showing a relatively

Table 2. Lattice Parameters and Unit Cell Volume of the Experimental and Calculated Relaxed Structures as Well as Average Bader Charges for Oxygen and Nickel at $x(\text{Li}) = 1.00, 0.75, 0.5,$ and 0.25 ⁵⁴

$x(\text{Li})$	$V (\text{\AA}^3)$		$a (\text{\AA})$		$c (\text{\AA})$		O charge lel	Ni charge lel
	DFT	XRD	DFT	XRD	DFT	XRD		
1.00	99.96	101.38(1)	2.91	2.8661(1)	13.63	14.249(1)	1.2	+1.38
0.75	99.05	100.64(1)	2.883	2.8421(1)	13.76	14.386(1)	1.1	+1.43
0.50	97.84	99.73(1)	2.855	2.8221(1)	13.86	14.460(1)	1.0	+1.47
0.25	93.39	94.26(2)	2.840	2.8153(1)	13.37	13.732(2)	0.8	+1.43

narrow peak at 528 eV (A1) and a broad peak from 535 to 550 eV (A2). A subtle peak indicated by an asterisk may be due to the presence of carbon black additive. To understand the evolution of the NCM811 spectra, let us first analyze the LiNiO₂ data. As is evident from Figure 5, the spectrum exhibits a distinct peak at 528 eV (α) and a broad absorption peak centered at 539 eV (β). The absorption arises as a result of transitions between the oxygen core level and unoccupied states in the conduction band. In LiNiO₂, the nickel ions are in the low spin 3d⁷ electron configuration ($t_{2g}^6 e_g^1$), while the O ions have fully occupied 2p states.⁴³ The unoccupied states probed by the K edge are located in the 2p level of oxygen hybridized with partially occupied 3d (α) and 4sp (β) levels of nickel.^{44,45} Accordingly, A1 and A2 in the NCM811 spectrum can be assigned to transitions of the oxygen core electron to the 2p oxygen level hybridized with 3d and 4sp transition metal bands, respectively. However, we note that nickel is subjected to Jahn–Teller distortion and partial charge disproportionation.⁴⁶ In LiNiO₂, these effects cause splitting of the 3d level of nickel into several states of similar energy, and eventually lead to peak broadening. In fact, A1 for pristine NCM811 shows such broadening, with a shoulder to high photon energy. Nevertheless, A1 is narrower than α in the LiNiO₂ spectrum, which indicates that both cobalt and manganese dilute nickel partially (as expected), thereby reducing Jahn–Teller activity and/or charge disproportionation.

As is seen, both the shape and position of A2 do not change notably with delithiation. This agrees with the fact that the oxygen 2p level, together with the empty transition metal 4sp orbitals, does not participate in the redox process. In contrast, the A1 peak intensity increases nearly linearly with decreasing lithium content due to depopulation of the 3d states of nickel during its oxidation (see also Figure S6). This result is consistent with the hXAS data described above. In the initial state, nickel has a filled t_{2g} level and an e_g level containing one electron.^{47,48} Transition to the final oxidized state upon delithiation requires depopulation of the e_g level by about one electron. Because the e_g orbitals, d_z^2 and $d_{x^2-y^2}$, directly point toward the ligands (octahedral symmetry), they can mix (σ type overlap) with the p_z orbitals of oxygen if they match in energy. The fact that A1 is strong and distinct suggests considerable mixing for the pristine NCM811 material already, like in the case of LiNiO₂, and the increase in peak intensity further implies charge transfer between the 3d states of nickel and 2p states of oxygen. Consequently, delithiation may result in depopulation not only of the e_g orbitals of nickel, but also of the p_z orbitals of oxygen, which inevitably affects the effective charge on the oxygen atoms.

Oxygen Charge Evolution. To shed more light on the charge evolution, DFT calculations with projector augmented wave (PAW) method were performed as implemented in the VASP code.^{49,50} Li _{x} NiO₂ was chosen as a model system for NCM811, where $x(\text{Li})$ was varied in the range 1.0–0.25 (see

Figures S7 and S8 for model geometries and calculated density of states [DOS]). The structures were based on the experimental XRD results, and the geometries were consequently fully optimized (including volume relaxation). Table 2 shows that the unit cell volume of the calculated relaxed structures (V_{DFT}) is smaller by up to 1.9% than that of the experimental structures (V_{XRD}). However, the results are reliable and the nonmonotonic behavior of the lattice along the z direction (changes in c lattice parameter) with decreasing lithium content is well reproduced by the calculations. Thus, implementation issues of the relaxation procedure can be ruled out.

The calculated average Bader charges for nickel and oxygen range from +1.38 to +1.47 and from –1.2 to –0.8, respectively. The charge on the nickel atoms increases from initially +1.38 to +1.47 at $x(\text{Li}) = 0.5$ and then slightly decreases to +1.43 at $x(\text{Li}) = 0.25$. The charge on the oxygen atoms varies from –1.2 to –0.8, with the change being greatest when $x(\text{Li})$ decreases from 0.5 to 0.25. These trends toward more positive charge reveal an evident decrease in electron density on both the nickel and oxygen atoms with delithiation. The nonmonotonic change in nickel charge (break of the positive trend when $x(\text{Li}) < 0.5$) is indicative of charge transfer from oxygen to nickel at low lithium content. Accordingly, the collapse of the Li O slabs at $x(\text{Li}) < 0.5$ (and the related shrinkage in interlayer spacing) can be understood in terms of the effective charge on the oxygen atoms. The size (height) of the Li O slabs directly depends on the degree of repulsion between the negatively charged oxygen planes.^{9,15} Large amounts of lithium initially screen the negative oxygen charge. The screening effect decreases with delithiation, leading to an increase in oxygen repulsion and expansion of the Li O slabs from 2.639(1) to 2.889(2) Å at $x(\text{Li}) = 0.5$. Further delithiation of the NCM cathode material results in further decrease of the screening effect, and it would be reasonable to expect an even larger expansion of the Li O slabs. Instead, the slab height decreases to 2.767(1) Å, even though lithium does not effectively screen the negative oxygen charge anymore. Overall, this indicates that the shrinkage is triggered by depletion of the negative charge on the oxygen atoms. The sXAS data establish considerable mixing between the 2p orbitals of oxygen and the partially filled e_g orbitals of nickel. This overlap induces charge transfer, which ultimately leads to collapse of the layered NCM structure. In this context, we note that our DFT results agree with previous experimental observations of thermal and electrochemical LiNiO₂ degradation.^{51–53} These studies reported a facile transition of layered Li _{x} NiO₂ to NiO type rock salt phases, thus demonstrating the intrinsic instability of the Ni^{3/4+}–O^{2–} configuration. Both at high states of charge and at high temperatures, the negative charge transfer from oxygen to nickel results in release of gaseous oxygen and formation of a stable NiO phase.

■ CONCLUSION

Here we investigated structural and electronic changes of NCM811 upon delithiation by means of *operando* and *ex situ* X ray diffraction, X ray absorption spectroscopy, and density functional theory calculations. Galvanostatic cycling tests showed that operation of the cathode material in the high voltage range ($E > 4.2$ V vs Li^+/Li and $x(\text{Li}) < 0.5$) causes accelerated capacity degradation. X ray diffraction revealed a large decrease in unit cell volume due to collapse of the layered lattice structure (severe shrinkage of the interlayer spacing) when $x(\text{Li}) < 0.5$. Transition metal K edge and L edge X ray absorption data confirmed the contribution of nickel to the charge compensation, resulting in shrinkage of the transition metal–oxygen layer. Soft X ray absorption spectroscopy indicated large mixing between the 2p orbitals of oxygen and the partially filled e_g orbitals of nickel, while results from density functional theory calculations demonstrated that this mixing induces charge transfer resulting in depletion of the effective oxygen charge and causing collapse of the layered NCM structure. Collectively, our findings emphasize the importance of the electronic mixing in nickel–oxygen states for maintaining the crystalline lattice and further suggest paying more attention to the transition metal–oxygen bonding when designing future cathode materials for high voltage operation.

■ ASSOCIATED CONTENT

● Supporting Information

The Supporting Information is available free of charge on the ACS Publications website at DOI: 10.1021/acs.jpcc.7b06598.

NCM811 full cell performance; additional XRD, hXAS, and sXAS data; and details on the DFT calculations, including VASP POSCAR data (PDF)

■ AUTHOR INFORMATION

Corresponding Authors

*Phone: +49 721 60826870. E mail: alexander.kondrakov@gmail.com.

*Phone: +49 721 60828827. E mail: torsten.brezesinski@kit.edu.

ORCID

Aleksandr O. Kondrakov: 0000 0003 1465 2854

Torsten Brezesinski: 0000 0002 4336 263X

Notes

The authors declare no competing financial interest.

■ ACKNOWLEDGMENTS

This study is part of the projects being funded within the BASF International Network for Batteries and Electrochemistry. Parts of this research were carried out at the light source PETRA III at DESY, a member of the Helmholtz Association (HGF). We thank Roman Chernikov for assistance in using beamline P65. We thank HZB for the allocation of synchrotron radiation beamtime and gratefully acknowledge the help of Aleksei Konashuk, Dmitry Smirnov, and Dong Zhou.

■ REFERENCES

(1) Schipper, F.; Erickson, E. M.; Erk, C.; Shin, J. Y.; Chesneau, F. F.; Aurbach, D. Review Recent Advances and Remaining Challenges for Lithium Ion Battery Cathodes: I. Nickel Rich, $\text{LiNi}_x\text{Co}_y\text{Mn}_z\text{O}_2$. *J. Electrochem. Soc.* **2017**, *164*, A6220–A6228.

(2) Noh, H. J.; Youn, S.; Yoon, C. S.; Sun, Y. K. Comparison of the Structural and Electrochemical Properties of Layered $\text{Li}[\text{Ni}_x\text{Co}_y\text{Mn}_z]\text{O}_2$ ($x = 1/3, 0.5, 0.6, 0.7, 0.8$ and 0.85) Cathode Material for Lithium Ion Batteries. *J. Power Sources* **2013**, *233*, 121–130.

(3) Manthiram, A.; Song, B.; Li, W. A Perspective on Nickel Rich Layered Oxide Cathodes for Lithium Ion Batteries. *Energy Stor. Mater.* **2017**, *6*, 125–139.

(4) Ishidzu, K.; Oka, Y.; Nakamura, T. Lattice Volume Change during Charge/Discharge Reaction and Cycle Performance of $\text{Li}[\text{Ni}_x\text{Co}_y\text{Mn}_z]\text{O}_2$. *Solid State Ionics* **2016**, *288*, 176–179.

(5) Kondrakov, A. O.; Schmidt, A.; Xu, J.; Geßwein, H.; Mönig, R.; Hartmann, P.; Sommer, H.; Brezesinski, T.; Janek, J. Anisotropic Lattice Strain and Mechanical Degradation of High and Low Nickel NCM Cathode Materials for Li Ion Batteries. *J. Phys. Chem. C* **2017**, *121*, 3286–3294.

(6) Ghanty, C.; Markovsky, B.; Erickson, E. M.; Talianker, M.; Haik, O.; Tal Yossef, Y.; Mor, A.; Aurbach, D.; Lampert, J.; Volkov, A.; et al. Li^+ Ion Extraction/Insertion of Ni Rich $\text{Li}_{1+x}(\text{Ni}_y\text{Co}_z\text{Mn}_w)\text{O}_2$ ($0.005 < x < 0.03$; $y:z = 8:1$, $w \approx 1$) Electrodes: In Situ XRD and Raman Spectroscopy Study. *ChemElectroChem* **2015**, *2*, 1479–1486.

(7) Li, J.; Petibon, R.; Glazier, S.; Sharma, N.; Pang, W. K.; Peterson, V. K.; Dahn, J. R. In Situ Neutron Diffraction Study of a High Voltage $\text{Li}(\text{Ni}_{0.42}\text{Mn}_{0.42}\text{Co}_{0.16})\text{O}_2/\text{Graphite}$ Pouch Cell. *Electrochim. Acta* **2015**, *180*, 234–240.

(8) Li, J.; Shunmugasundaram, R.; Doig, R.; Dahn, J. R. In Situ X Ray Diffraction Study of Layered Li Ni Mn Co Oxides: Effect of Particle Size and Structural Stability of Core Shell Materials. *Chem. Mater.* **2016**, *28*, 162–171.

(9) Van der Ven, A.; Aydinol, M. K.; Ceder, G.; Kresse, G.; Hafner, J. First Principles Investigation of Phase Stability in Li_xCoO_2 . *Phys. Rev. B: Condens. Matter Mater. Phys.* **1998**, *58*, 2975–2987.

(10) Yin, S. C.; Rho, Y. H.; Swainson, I.; Nazar, L. F. X Ray/Neutron Diffraction and Electrochemical Studies of Lithium De/Re Intercalation in $\text{Li}_{1-x}\text{Co}_{1/3}\text{Ni}_{1/3}\text{Mn}_{1/3}\text{O}_2$ ($x = 0 \rightarrow 1$). *Chem. Mater.* **2006**, *18*, 1901–1910.

(11) Delmas, C.; Peres, J. P.; Rougier, A.; Demourgues, A.; Weill, F.; Chadwick, A.; Broussely, M.; Perton, F.; Biensan, Ph.; Willmann, P. On the Behavior of the Li_xNiO_2 System: An Electrochemical and Structural Overview. *J. Power Sources* **1997**, *68*, 120–125.

(12) Liao, P. Y.; Duh, J. G.; Sheu, H. S. In Situ Synchrotron X Ray Studies of $\text{LiNi}_{1-x-y}\text{Co}_y\text{Mn}_x\text{O}_2$ Cathode Materials. *Electrochem. Solid State Lett.* **2007**, *10*, A88–A92.

(13) Liao, P. Y.; Duh, J. G.; Lee, J. Fu. Valence Change and Local Structure during Cycling of Layer Structured Cathode Materials. *J. Power Sources* **2009**, *189*, 9–15.

(14) Petersburg, C. F.; Li, Z.; Chernova, N. A.; Whittingham, M. S.; Alamgir, F. M. Oxygen and Transition Metal Involvement in the Charge Compensation Mechanism of $\text{LiNi}_{1/3}\text{Mn}_{1/3}\text{Co}_{1/3}\text{O}_2$ Cathodes. *J. Mater. Chem.* **2012**, *22*, 19993–20000.

(15) Tsai, Y. W.; Hwang, B. J.; Ceder, G.; Sheu, H. S.; Liu, D. G.; Lee, J. F. In Situ X Ray Absorption Spectroscopic Study on Variation of Electronic Transitions and Local Structure of $\text{LiNi}_{1/3}\text{Co}_{1/3}\text{Mn}_{1/3}\text{O}_2$ Cathode Material during Electrochemical Cycling. *Chem. Mater.* **2005**, *17*, 3191–3199.

(16) Kosova, N. V.; Devyatkina, E. T.; Kaichev, V. V.; Kellerman, D. G. Effect of Electronic State of Ions on the Electrochemical Properties of Layered Cathode Materials $\text{LiNi}_{1-2x}\text{Co}_x\text{Mn}_x\text{O}_2$. *Russ. J. Electrochem.* **2008**, *44*, 543–549.

(17) Seo, D. H.; Urban, A.; Ceder, G. Calibrating Transition Metal Energy Levels and Oxygen Bands in First Principles Calculations: Accurate Prediction of Redox Potentials and Charge Transfer in Lithium Transition Metal Oxides. *Phys. Rev. B: Condens. Matter Mater. Phys.* **2015**, *92*, 115118.

(18) Yoon, W. S.; Kim, K. B.; Kim, M. G.; Lee, M. K.; Shin, H. J.; Lee, J. M.; Lee, J. S.; Yo, C. H. Oxygen Contribution on Li Ion Intercalation Deintercalation in LiCoO_2 Investigated by O K Edge and Co L Edge X ray Absorption Spectroscopy. *J. Phys. Chem. B* **2002**, *106*, 2526–2532.

- (19) Chen, C. H.; Hwang, B. J.; Chen, C. Y.; Hu, S. K.; Chen, J. M.; Sheu, H. S.; Lee, J. F. Soft X Ray Absorption Spectroscopy Studies on the Chemically Delithiated Commercial LiCoO₂ Cathode Material. *J. Power Sources* **2007**, *174*, 938–943.
- (20) Hollmark, H. M.; Duda, L. C.; Dahbi, M.; Saadoune, I.; Gustafsson, T.; Edström, K. Resonant Soft X Ray Emission Spectroscopy and X Ray Absorption Spectroscopy on the Cathode Material LiNi_{0.65}Co_{0.25}Mn_{0.1}O₂. *J. Electrochem. Soc.* **2010**, *157*, A962–A966.
- (21) Yoon, W. S.; Balasubramanian, M.; Chung, K. Y.; Yang, X. Q.; McBreen, J.; Grey, C. P.; Fischer, D. A. Investigation of the Charge Compensation Mechanism on the Electrochemically Li Ion Deintercalated Li_{1-x}Co_{1/3}Ni_{1/3}Mn_{1/3}O₂ Electrode System by Combination of Soft and Hard X Ray Absorption Spectroscopy. *J. Am. Chem. Soc.* **2005**, *127*, 17479–17487.
- (22) Hy, S.; Su, W. N.; Chen, J. M.; Hwang, B. J. Soft X Ray Absorption Spectroscopic and Raman Studies on Li_{1.2}Ni_{0.2}Mn_{0.6}O₂ for Lithium Ion Batteries. *J. Phys. Chem. C* **2012**, *116*, 25242–25247.
- (23) Oishi, M.; Fujimoto, T.; Takanashi, Y.; Orikasa, Y.; Kawamura, A.; Ina, T.; Yamashige, H.; Takamatsu, D.; Sato, K.; Murayama, H.; et al. Charge Compensation Mechanisms in Li_{1.16}Ni_{0.15}Co_{0.19}Mn_{0.50}O₂ Positive Electrode Material for Li Ion Batteries Analyzed by a Combination of Hard and Soft X Ray Absorption Near Edge Structure. *J. Power Sources* **2013**, *222*, 45–51.
- (24) Chen, J. G. NEXAFS Investigations of Transition Metal Oxides, Nitrides, Carbides, Sulfides and Other Interstitial Compounds. *Surf. Sci. Rep.* **1997**, *30*, 1–152.
- (25) de Biasi, L.; Lieser, G.; Rana, J.; Indris, S.; Dräger, C.; Glatthaar, S.; Mönig, R.; Ehrenberg, H.; Schumacher, G.; Binder, J. R.; et al. Unravelling the Mechanism of Lithium Insertion into and Extraction from Trirutile Type LiNiFeF₆ Cathode Material for Li Ion Batteries. *CrystEngComm* **2015**, *17*, 6163–6174.
- (26) Ravel, B.; Newville, M. ATHENA, ARTEMIS, HEPHAESTUS: Data Analysis for X Ray Absorption Spectroscopy using IFEFFIT. *J. Synchrotron Radiat.* **2005**, *12*, 537–541.
- (27) Molodtsov, S. L.; Fedoseenko, S. I.; Vyalikh, D. V.; Iossifov, I. E.; Follath, R.; Gorovikov, S. A.; Brzhezinskaya, M. M.; Dedkov, Y. S.; Püttner, R.; Schmidt, J. S.; et al. High Resolution Russian German Beamline at BESSY. *Appl. Phys. A: Mater. Sci. Process.* **2009**, *94*, 501–505.
- (28) Perdew, J. P.; Burke, K.; Ernzerhof, M. Generalized Gradient Approximation Made Simple. *Phys. Rev. Lett.* **1996**, *77*, 3865–3868.
- (29) Monkhorst, H. J.; Pack, J. D. Special Points for Brillouin Zone Integrations. *Phys. Rev. B* **1976**, *13*, 5188–5192.
- (30) Grimme, S. Semiempirical GGA Type Density Functional Constructed with a Long Range Dispersion Correction. *J. Comput. Chem.* **2006**, *27*, 1787–1799.
- (31) Fringant, C.; Tranchant, A.; Messina, R. Behavior of Lithium Electrolyte Interface during Cycling in Some Ether Carbonate and Carbonate Mixtures. *Electrochim. Acta* **1995**, *40*, 513–523.
- (32) Hwang, S.; Chang, W.; Kim, S. M.; Su, D.; Kim, D. H.; Lee, J. Y.; Chung, K. Y.; Stach, E. A. Investigation of Changes in the Surface Structure of Li_xNi_{0.8}Co_{0.15}Al_{0.05}O₂ Cathode Materials Induced by the Initial Charge. *Chem. Mater.* **2014**, *26*, 1084–1092.
- (33) Li, W.; Reimers, J. N.; Dahn, J. R. In Situ X Ray Diffraction and Electrochemical Studies of Li_{1-x}NiO₂. *Solid State Ionics* **1993**, *67*, 123–130.
- (34) Croguennec, L.; Pouillier, C.; Mansour, A. N.; Delmas, C. Structural Characterisation of the Highly Deintercalated Li_xNi_{1.02}O₂ Phases (with $x \leq 0.30$). *J. Mater. Chem.* **2001**, *11*, 131–141.
- (35) Hwang, B. J.; Tsai, Y. W.; Carlier, D.; Ceder, G. A Combined Computational/Experimental Study on LiNi_{1/3}Co_{1/3}Mn_{1/3}O₂. *Chem. Mater.* **2003**, *15*, 3676–3682.
- (36) Deb, A.; Bergmann, U.; Cramer, S. P.; Cairns, E. J. In Situ X Ray Absorption Spectroscopic Study of the Li[Ni_{1/3}Co_{1/3}Mn_{1/3}]O₂ Cathode Material. *J. Appl. Phys.* **2005**, *97*, 113523.
- (37) Yabuuchi, N.; Kumar, S.; Li, H. H.; Kim, Y. T.; Shao Horn, Y. Changes in the Crystal Structure and Electrochemical Properties of Li_xNi_{0.5}Mn_{0.5}O₂ during Electrochemical Cycling to High Voltages. *J. Electrochem. Soc.* **2007**, *154*, A566–A578.
- (38) Dixit, M.; Kosa, M.; Lavi, O. S.; Markovsky, B.; Aurbach, D.; Major, D. T. Thermodynamic and Kinetic Studies of Li Ni_{0.5}Co_{0.2}Mn_{0.3}O₂ as a Positive Electrode Material for Li Ion Batteries Using First Principles. *Phys. Chem. Chem. Phys.* **2016**, *18*, 6799–6812.
- (39) Cherkashinin, G.; Motzko, M.; Schulz, N.; Späth, T.; Jaegermann, W. Electron Spectroscopy Study of Li[Ni,Co,Mn]O₂/Electrolyte Interface: Electronic Structure, Interface Composition, and Device Implications. *Chem. Mater.* **2015**, *27*, 2875–2887.
- (40) Xiao, J.; Chernova, N. A.; Whittingham, M. S. Layered Mixed Transition Metal Oxide Cathodes with Reduced Cobalt Content for Lithium Ion Batteries. *Chem. Mater.* **2008**, *20*, 7454–7464.
- (41) Yoon, W. S.; Chung, K. Y.; McBreen, J.; Fischer, D. A.; Yang, X. Q. Electronic Structural Changes of the Electrochemically Li Ion Deintercalated LiNi_{0.8}Co_{0.15}Al_{0.05}O₂ Cathode Material Investigated by X Ray Absorption Spectroscopy. *J. Power Sources* **2007**, *174*, 1015–1020.
- (42) Fano, U.; Cooper, J. W. Spectral Distribution of Atomic Oscillator Strengths. *Rev. Mod. Phys.* **1968**, *40*, 441–507.
- (43) Petit, L.; Stocks, G. M.; Egami, T.; Szotek, Z.; Temmerman, W. M. Ground State Valency and Spin Configuration of the Ni Ions in Nickelates. *Phys. Rev. Lett.* **2006**, *97*, 146405.
- (44) Yoon, W. S.; Chung, K. Y.; McBreen, J.; Fischer, D. A.; Yang, X. Q. Changes in Electronic Structure of the Electrochemically Li Ion Deintercalated LiNiO₂ System Investigated by Soft X Ray Absorption Spectroscopy. *J. Power Sources* **2006**, *163*, 234–237.
- (45) de Groot, F. M. F.; Grioni, M.; Fuggle, J. C.; Ghijsen, J.; Sawatzky, G. A.; Petersen, H. Oxygen 1s X Ray Absorption Edges of Transition Metal Oxides. *Phys. Rev. B: Condens. Matter Mater. Phys.* **1989**, *40*, 5715–5723.
- (46) Chen, H.; Freeman, C. L.; Harding, J. H. Charge Disproportionation and Jahn Teller Distortion in LiNiO₂ and NaNiO₂: A Density Functional Theory Study. *Phys. Rev. B: Condens. Matter Mater. Phys.* **2011**, *84*, 085108.
- (47) Rougier, A.; Chadwick, A. V.; Delmas, C. XAS Study of Lithium Nickel Oxide. *Nucl. Instrum. Methods Phys. Res., Sect. B* **1995**, *97*, 75–77.
- (48) Rougier, A.; Delmas, C.; Chadwick, A. V. Non Cooperative Jahn Teller Effect in LiNiO₂: An EXAFS Study. *Solid State Commun.* **1995**, *94*, 123–127.
- (49) Blöchl, P. E. Projector Augmented Wave Method. *Phys. Rev. B: Condens. Matter Mater. Phys.* **1994**, *50*, 17953–17979.
- (50) Kresse, G.; Hafner, J. Ab Initio Molecular Dynamics for Liquid Metals. *Phys. Rev. B: Condens. Matter Mater. Phys.* **1993**, *47*, 558–561.
- (51) Antolini, E. Li_xNi_{1-x}O (0 < x ≤ 0.3) Solid Solutions: Formation, Structure and Transport Properties. *Mater. Chem. Phys.* **2003**, *82*, 937–948.
- (52) Kanno, R.; Kubo, H.; Kawamoto, Y.; Kamiyama, T.; Izumi, F.; Takeda, Y.; Takano, M. Phase Relationships and Lithium Deintercalation in Lithium Nickel Oxides. *J. Solid State Chem.* **1994**, *110*, 216–225.
- (53) Xu, J.; Lin, F.; Doeff, M. M.; Tong, W. A Review of Ni Based Layered Oxides for Rechargeable Li Ion Batteries. *J. Mater. Chem. A* **2017**, *5*, 874–901.
- (54) Tang, W.; Sanville, E.; Henkelman, G. A Grid Based Bader Analysis Algorithm without Lattice Bias. *J. Phys.: Condens. Matter* **2009**, *21*, 084204.